



RESEARCH ARTICLE

10.1002/2016JF003878

Cross-shore sand transport by infragravity waves as a function of beach steepness

Key Points:

- Relative IG height is a good indicator for sand suspension mechanism, IG transport direction, and relative importance
- For low relative IG height, sand transport is related to correlation of IG orbital motion with sea-swell wave envelope
- For large relative IG height, sand is suspended during offshore IG velocities and relatively important to total transport

Correspondence to:

A. T. M. de Bakker,
a.t.m.debakker@uu.nl

Citation:

de Bakker, A. T. M., J. A. Brinkkemper, F. van der Steen, M. F. S. Tissier, and B. G. Ruessink (2016), Cross-shore sand transport by infragravity waves as a function of beach steepness, *J. Geophys. Res. Earth Surf.*, 121, doi:10.1002/2016JF003878.

Received 8 MAR 2016

Accepted 18 SEP 2016

Accepted article online 27 SEP 2016

A. T. M. de Bakker^{1,2}, J. A. Brinkkemper¹, F. van der Steen¹, M. F. S. Tissier³, and B. G. Ruessink¹

¹Department of Physical Geography, Faculty of Geosciences, Utrecht University, Utrecht, Netherlands, ²Now at LIENSs CNRS-Université de La Rochelle, Institut du Littoral et de l'Environnement, La Rochelle, France, ³Environmental Fluid Mechanics Section, Faculty of Civil Engineering and Geosciences, Delft University of Technology, Delft, Netherlands

Abstract Two field data sets of near-bed velocity, pressure, and sediment concentration are analyzed to study the influence of infragravity waves on sand suspension and cross-shore transport. On the moderately sloping Sand Motor beach ($\approx 1:35$), the local ratio of infragravity wave height to sea-swell wave height is relatively small ($H_{IG}/H_{SW} < 0.4$), and sand fluxes are related to the correlation of the infragravity-wave orbital motion with the sea-swell wave envelope, r_0 . When the largest sea-swell waves are present during negative infragravity velocities (bound wave, negative correlation r_0), most sand is suspended here, and the infragravity sand flux q_{IG} is offshore. When r_0 is positive, the largest sea-swell waves are present during positive infragravity velocities (free wave), and q_{IG} is onshore directed. For both cases, the infragravity contribution to the total sand flux is, however, relatively small ($< 20\%$). In the inner surf zone of the gently ($\approx 1:80$) sloping Ameland beach, the infragravity waves are relatively large ($H_{IG}/H_{SW} > 0.4$), most sand is suspended during negative infragravity velocities, and q_{IG} is offshore directed. The infragravity contribution to the total sand flux is considerably larger and reaches up to $\approx 60\%$ during energetic conditions. On the whole, H_{IG}/H_{SW} is a good indicator for the infragravity-related sand suspension mechanism and the resulting infragravity sand transport direction and relative importance.

1. Introduction

Cross-shore sand transport on (approximately) alongshore uniform beaches results from oscillatory wave motions and the wave-averaged mean current (undertow). Oscillatory transport by sea-swell waves ($\approx 2-20$ s) is often directed onshore due to velocity skewness and asymmetry [e.g., King, 1991; Elgar et al., 2001; Van der A et al., 2010; Ruessink et al., 2011; Miles, 2013]. The offshore-directed undertow is the main mechanism inducing offshore-directed transport [e.g., Gallagher et al., 1998; Ruessink et al., 1998a] and depends partly on the beach slope; for given wave conditions, the undertow is stronger on steeper beaches [Longuet-Higgins, 1983; Aagaard et al., 2002; Walstra et al., 2016], as breaking is locally more intense. Infragravity waves (20–200 s), which receive their energy through nonlinear energy transfers from sea-swell waves, can also induce cross-shore sand transport (q_{IG}). Existing studies on sand suspension and flux by infragravity waves [e.g., Abdelrahman and Thornton, 1987; Beach and Sternberg, 1988; Roelvink and Stive, 1989; Shibayama et al., 1991; Osborne and Greenwood, 1992; Russell, 1993; Ruessink et al., 2000; Smith and Mocke, 2002; Conley and Beach, 2003; Aagaard and Greenwood, 2008; Baldock et al., 2010; Alsina and Cáceres, 2011; Aagaard et al., 2013; Kularatne and Pattiaratchi, 2014] have resulted in observations that contrast in direction and relative importance of q_{IG} , as well as in the underlying suspension mechanism. These contrasting observations are presumably because of the diversity in boundary conditions, such as the variety of beach profiles and offshore wave conditions. Understanding the role of infragravity waves in the suspension of sand, and the resulting cross-shore flux, is still a major challenge and is crucial in understanding the morphological change in the nearshore, especially during high-energy conditions [e.g., Russell, 1993; Van Thiel de Vries et al., 2008].

Both onshore and offshore sand transports have been observed at infragravity frequencies [e.g., Osborne and Greenwood, 1992; Russell, 1993; Smith and Mocke, 2002; Houser and Greenwood, 2005; Aagaard and Greenwood, 2008], and several processes have been suggested to explain the contradicting transport directions. Based on hydrodynamic data, Abdelrahman and Thornton [1987] and Roelvink and Stive [1989] proposed that as the infragravity wave is less energetic than sea-swell waves, the presence of the largest sea-swell waves during either negative infragravity velocities (u_{IG} , bound wave) or positive u_{IG} (free wave) could potentially explain

©2016. The Authors.

This is an open access article under the terms of the Creative Commons Attribution-NonCommercial-NoDerivs License, which permits use and distribution in any medium, provided the original work is properly cited, the use is non-commercial and no modifications or adaptations are made.

the dominant location of suspension, and thereby the resulting infragravity transport direction. This relative location can be described by the correlation r_0 between the sea-swell wave envelope and u_{IG} . In the shoaling zone and outer part of the surf zone, larger (breaking) sea-swell waves are present during the negative u_{IG} , and r_0 is negative. Consequently, net infragravity sand transports are directed offshore [Larsen, 1982; Huntley and Hanes, 1987; Osborne and Greenwood, 1992; Ruessink et al., 1998a; Smith and Mocke, 2002]. In the inner surf zone, where infragravity waves modulate the sea-swell wave height (by locally raising or lowering the water level) [e.g., Abdelrahman and Thornton, 1987; Tissier et al., 2015], the larger sea-swell waves are present during positive u_{IG} , and r_0 is positive. Consequently, they suspend more sand during positive u_{IG} , providing a net onshore transport at infragravity-wave timescale. Other studies, where infragravity waves dominated the water motion in the inner surf zone, observed infragravity waves to suspend sand as well [e.g., Beach and Sternberg, 1988; Russell, 1993]. During these conditions, sand was predominantly suspended during negative u_{IG} , resulting in an offshore infragravity transport.

Infragravity waves can dominate the inner surf and swash zones due to both their increase in height toward the shore through shoaling, and energy transfer from sea-swell waves, and most importantly because sea-swell waves have here already largely dissipated. This is particularly true during high-energy conditions and on mild slopes [e.g., Guza and Thornton, 1982; Ruessink et al., 1998b; Sénéchal et al., 2011; De Bakker et al., 2015]. We hypothesize that the relative importance of infragravity-wave height to sea-swell wave height, which is affected by beach characteristics, the location in the surf zone, and offshore wave conditions, determines which of the above mentioned sand suspension processes dominates and can hereby explain the reported contrasting infragravity sand flux directions. Here we test this hypothesis by analyzing two field data sets obtained on a gently ($\approx 1:80$) and a moderately ($\approx 1:35$) sloping beach, both located in the Netherlands. First, we introduce the field sites, measurement conditions, and the initial data processing. In section 3, we investigate our hypothesis by exploring trends in infragravity-wave-induced sand suspension and transport. In section 4, we discuss the effects of sensor height, and we bring the observed trends together in a conceptual picture. The main conclusions are given in section 5.

2. Methods

2.1. Field Sites and Instrument Array

Field observations of near-bed pressure, velocity, and suspended sand concentrations were collected on two micromesotidal beaches in the Netherlands. One campaign took place in autumn 2010 on the gently sloping ($\approx 1:80$) Ballum beach (Figure 1), located on the barrier island Ameland [Ruessink et al., 2012; De Bakker et al., 2014]. The other campaign was in autumn 2014 on the moderately sloping ($\approx 1:35$) Sand Motor beach, a 21 Mm³ nourishment near Ter Heijde (Figure 1) [see De Schipper et al., 2016]. During both 6 week campaigns a cross-shore instrument array was placed in the intertidal zone, ranging from the spring low-tide water level to just above the spring high-tide water level to also ensure measurements on the higher part of the beach during high energetic conditions. Three frames were placed that were each equipped with an electromagnetic flowmeter (EMF), a pressure transducer (PT), and three Seapoint optical backscatter sensors (OBSs), all sampling continuously at 4 Hz (locations P5, P8, and P10 at the Sand Motor and P7, P9, and P11 at Ameland). At Ameland, an additional frame was placed (location P5) that was equipped with a PT (sampling at 4 Hz), three Sontek Acoustic Doppler Velocimeter Ocean probes (sampling at 10 Hz), and an OBS array consisting of five sensors (sampling at 4 Hz). The PTs were placed at 5–10 cm above the bed, the EMFs at 15–20 cm above the bed, and the OBSs at 3–20 cm above the bed. In between the frames, stand-alone PTs were placed that sampled continuously at 5 Hz. The instrument heights were readjusted daily because of variations in bed level. The beach profiles were measured various times with real-time kinematic GPS during the Ameland campaign and daily at the Sand Motor. The bed material had a median grain size of around 200 μm on Ameland and 400 μm at the Sand Motor. Both beaches were approximately alongshore uniform during the respective campaigns, and no sign of rip currents was observed near the arrays.

The offshore wave conditions (significant wave height H_0 , period T_0 and angle of incidence θ_0) during the Ameland campaign were measured by a directional buoy positioned in 24 m water depth. The offshore water level fluctuations (η_0) were measured some 20 km to the west of the field site, at the tidal station Terschelling Noordzee. Offshore wave conditions during the Sand Motor campaign were measured by a directional buoy located in 11 m water depth, about 0.8 km seaward of the field site. The offshore water level fluctuations were obtained by averaging the η_0 values of the tidal stations Hoek van Holland and Scheveningen, located some 10 km south and north of the Sand Motor, respectively.

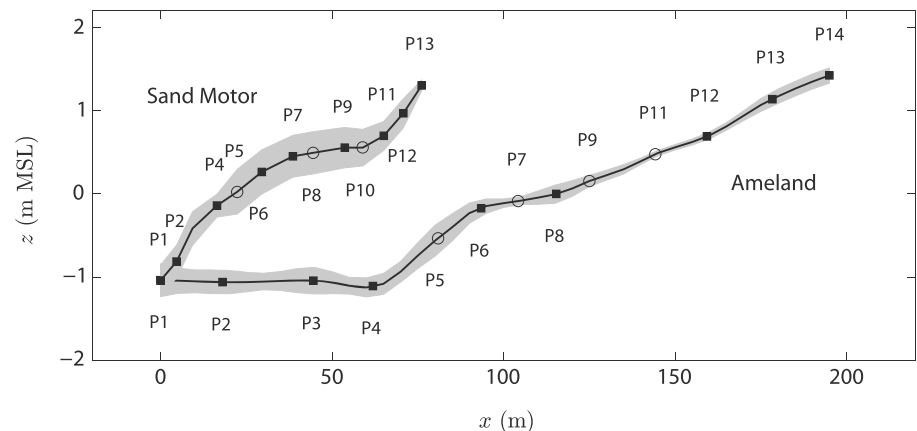


Figure 1. The campaign mean bed elevation z with respect to mean sea level versus cross-shore distance x for Ameland and the Sand Motor. The gray region is the bathymetry standard deviation over time. Black filled squares indicate the PTs; open circles indicate collocated EMFs, OBSs, and PTs. The ADV0 rig at Ameland was positioned at P5. At both sites $x = 0$ was taken at P1, the most seaward PT. P3 malfunctioned at the Sand Motor campaign and is not shown here.

2.2. Data Processing

Around each high tide, a period of 2 h was selected when wave characteristics and water levels at the array were approximately stationary. The pressure data were, after correction for air pressure, converted to free sea-surface elevation using linear wave theory. Sensor heights with respect to the bed were measured manually during low tide and were linearly interpolated to determine the sensor heights during high tide. The sea-surface elevation and velocity signals were quadratically detrended and, when needed, resampled to 4 Hz. These were then band pass filtered into infragravity (0.005–0.05 Hz) and sea-swell frequencies (0.05–1 Hz). Sea-surface elevations were processed per blocks of 30 min into water depth h , and into significant sea-swell wave height H_{sw} , and significant infragravity-wave height H_{IG} using standard spectral analysis. When part of the sea-surface elevation and velocity time series showed alternately dry and wet conditions, the complete series was removed. High tides with alongshore-velocity variance in the infragravity band exceeding 75% of the cross-shore infragravity velocity variance were removed from both data sets. Shear wave energy contribution (calculated following *Lippmann et al.* [1999]) did not exceed 75% of the total infragravity energy. Imposing limits for the shear wave energy contribution, as performed by *De Bakker et al.* [2014] for the hydrodynamical analysis of the Ameland data, was not critical to our present results and was therefore foregone here. In total, 71 two hour periods were retained in the Ameland data set and 55 in the Sand Motor data set.

OBSs are sensitive to both sediment properties [e.g., *Ludwig and Hanes*, 1990; *Conner and De Visser*, 1992; *Russell*, 1993; *Bunt et al.*, 1999] and air bubbles [e.g., *Smith and Mocke*, 2002; *Puleo et al.*, 2006], although for grain sizes between 200 and 400 μm the sensitivity is limited [*Conner and De Visser*, 1992]. Small spatial variations in grain size and sorting were here taken into account by calibrating each sensor separately with sand obtained at that particular cross-shore location. The OBSs were calibrated in a sediment recirculation tank, and the sensor output correlated quadratically with the sand concentration over the range from 0 to $\approx 40 \text{ kg/m}^3$ (for both data sets the correlation coefficient squared $r^2 = 0.99$). The latter value is the largest concentration that can be obtained reliably in our own facility. The curves were, however, applied to all sensor outputs, implying that concentration peaks in excess of 40 kg/m^3 are based on extrapolation. Application of the calibration curves often resulted in small ($< 0.1 \text{ kg/m}^3$) background concentrations. To remove this background level, the 0.5th percentile of a 15 min long concentration signal was determined and subsequently subtracted from the observations. The few subzero values were set to 0 kg/m^3 . Concentration time series were checked in two ways for the presence of air bubbles. First, when the concentration time series showed large, short-period spikes that fell directly back to a concentration of 0 kg/m^3 , the entire 2 h time series was removed from the data set. Furthermore, air bubbles raise the instantaneous sand concentrations high above the bed to values larger than those measured close to the bed. Whenever this occurred in a time series, during that particular high tide all sand concentration time series of that measurement location were removed from the data set. Finally, to improve comparisons between the different measurement conditions, concentration time series of the lowest OBS were used only when it was between 0.03 and 0.1 m above the bed. The dependence of the results on sensor height will be discussed in section 4.1. From the tides that were initially retained after the

hydrodynamic checks, at Ameland in total 29 high tides were retained with concentration data at at least one location. In more detail, 11 high tides were retained at location P5, 19 at P7, 21 at P9, and 15 at P11. At the Sand Motor, in total 29 tides were retained: 22 at location P5, 18 at P8, and 8 at P10. We will refer to all these tides as the selected high tides in the following sections.

2.3. Sand Fluxes

The cross-shore sand flux at a discrete sensor height is defined as the product of the instantaneous sand concentration c and cross-shore velocity u , where a positive value indicates onshore flux. The net time-averaged sand flux (q_{total}) consists of a mean (overbar) and oscillating (tilde) component:

$$q_{\text{total}} = \langle uc \rangle = \langle (\bar{u} + \tilde{u})(\bar{c} + \tilde{c}) \rangle = \bar{u}\bar{c} + \langle \tilde{u}\tilde{c} \rangle, \quad (1)$$

where the first term on the right-hand side is the local mean sand flux (q_{mean}), and $\langle \dots \rangle$ indicates a time-averaged value. The second term is the wave related, or oscillatory flux which is nonzero when fluctuations in u and c are correlated. It can be subdivided into a sea-swell (SW) and an infragravity wave (IG) component:

$$\langle \tilde{u}\tilde{c} \rangle = \langle (u_{\text{SW}} + u_{\text{IG}})(c_{\text{SW}} + c_{\text{IG}}) \rangle \approx \langle u_{\text{SW}} \cdot c_{\text{SW}} \rangle + \langle u_{\text{IG}} \cdot c_{\text{IG}} \rangle. \quad (2)$$

The two terms on the right-hand side are the sea-swell (q_{SW}) and infragravity (q_{IG}) frequency flux rate. The products of an SW and IG time series are neglected, as they are uncorrelated and therefore small compared with the other two components. Equations (1) and (2) can thus be written as

$$\langle uc \rangle = \bar{u}\bar{c} + \langle u_{\text{SW}} \cdot c_{\text{SW}} \rangle + \langle u_{\text{IG}} \cdot c_{\text{IG}} \rangle. \quad (3)$$

Values of q_{SW} , q_{IG} , and q_{mean} were computed for 30 min blocks. The relative contribution of q_{IG} to the sand flux rate was determined as $|q_{\text{IG}}|/(|q_{\text{IG}}| + |q_{\text{SW}}| + |q_{\text{mean}}|)$. Contributions of the other components were determined analogously. Although we measured u and c at different heights above the bed, we chose not to correct for this as effects for our data were estimated to be small (not shown) following the method of Ruessink *et al.* [1998a]. In addition, the exact sensor heights during high tide were not known.

To study the dependence of sand suspension events on the relative location of sea-swell waves, we determined the correlation r_0 between the sea-swell wave envelope A , and u_{IG} . We define the sea-swell wave envelope A by

$$A(t) = |u^{\text{SW}}(t) + i\Gamma\{u^{\text{SW}}\}|^{\text{IG}}, \quad (4)$$

where $i\Gamma$ denotes the Hilbert transform operator, and the superscript IG indicates band-pass filtering to the infragravity frequency range. The Hilbert transform applies a phase shift of $\pi/2$ on the signal it operates on, independent on frequency [e.g., Lancaster and Šaulkauskas, 1996].

2.4. Measured Conditions

During the Ameland campaign, offshore wave heights H_0 varied between 0.3 m and 5.9 m, and periods T_0 varied between 2.9 s and 7.9 s (Figures 2a and 2c). Two periods with storm conditions occurred, separated by rather mild conditions. Offshore significant wave heights reached 3.6 m during a storm of a few days at the beginning of the campaign. A second storm close to the end of the campaign persisted for about 1.5 weeks and caused offshore significant wave heights to increase up to 5.9 m. The presence of an ebbtidal delta a few kilometers seaward of the array caused the wave height to decrease substantially before reaching the measurement transect, with sea-swell wave heights reaching a maximum at P1 of only 1.7 m (Figure 2a). The angles of incidence θ_0 were either $<100^\circ$ or $>300^\circ$ at the east-west orientated beach at Ameland (shorenormal $\approx 358.2^\circ$), with predominantly northerly θ_0 (i.e., shore-normal approach) during the two storm periods (Figure 2e). At the Sand Motor, conditions were milder than at Ameland, with offshore significant wave heights varying between 0.1 and 4.9 m and wave periods between 2.7 and 7.7 s (Figures 2b and 2d). The only storm persisted for a few days and resulted in offshore significant wave heights up to 4.9 m and a surge of ≈ 1.5 m (Figure 2h). Wave heights decreased only slightly before reaching P1, with a maximum of 2.4 m during the storm. The angles of incidence were $275^\circ < \theta_0 < 350^\circ$ at the approximately northwest-southeast oriented flank of the Sand Motor (shorenormal $\approx 293^\circ$). The tidal range at Ameland was about 3 m, a meter larger than at the Sand Motor (Figures 2g and 2h).

At Ameland, the H_0 ranged between 0.7 and 4.4 m during the selected high tides, and T_0 ranged between 3.1 and 7.0 s. At the Sand Motor, during the selected tides, H_0 varied from 0.3 m to 4.3 m, and T_0 between

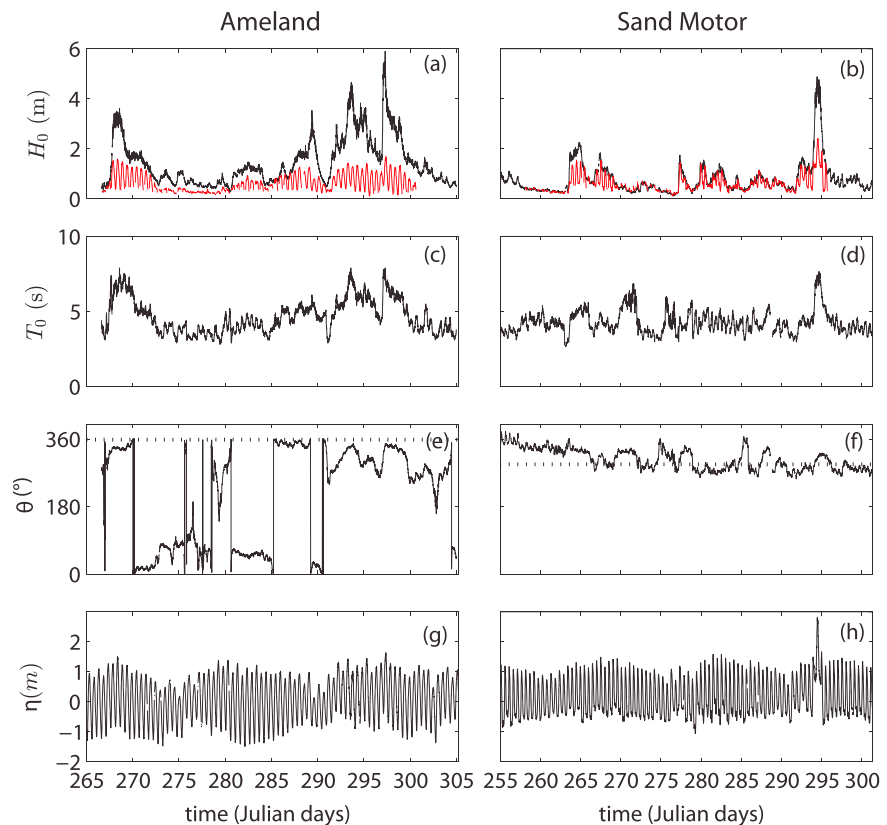


Figure 2. (a) Significant wave height, offshore (black) and at P1 (red), (c) offshore wave period T_0 , (e) offshore angle of incidence θ with respect to north, and (g) water level η_0 versus time at Ameland (Figures 2a, c, e, and g) and the (b, d, f and h) Sand Motor. The dotted lines in Figures 2e and 2f represent the shore normal direction.

3.1 and 7.1 s. The significant infragravity wave height H_{IG} at the most seaward positioned sensor varied between 0.08 and 0.48 m at Ameland and 0.04 and 0.47 m at the Sand Motor (Figures 3a and 3b). At both field sites H_{IG} correlated well with H_0 , although some saturation can be seen at Ameland for $H_0 > 3$ m. The constant of proportionality m for the mean at all locations of both field sites was ≈ 0.13 . We note that we used quantile regression analysis [e.g., *Cade and Noon, 2003; Koehler, 2005*] in this paper to examine the (linear) relation between two variables. Quantile regression estimates multiple rates of change (slope) from the minimum to the maximum response and provides a more complete picture of the relation between the variables. It assesses unequal variations due to complex interactions that cannot all be measured and accounted for when only certain variables are plotted against each other. Especially for the sand flux data described below, quantile regression is more robust than ordinary least squares regression. Regression lines were computed for the 10%, 50%, and 90% quantiles, denoted as $\text{Tau} = 0.1, 0.5, \text{ and } 0.9$, respectively, to study the maximum, median, and minimum responses and to identify whether trends are statistically significant altogether. The 90% significance of all lines was estimated following *Koehler [2005]*. Especially at the gently sloping Ameland field site, infragravity waves became increasingly more important toward the shoreline, and during more energetic conditions even dominated the water motion (Figures 3c and 3d). On the Sand Motor the infragravity wave height was relatively small ($H_{IG}/H_{SW} = 0.1 - 0.5$) compared to Ameland ($H_{IG}/H_{SW} = 0.2 - 1$) (Figures 3c and 3d), even for high energetic conditions. Quantile regression lines for $\text{Tau} = 0.1$ and 0.5 were statistically significant, but not for $\text{Tau} = 0.9$. This dependence of infragravity-wave height on beach slope has been observed before by, for example, *De Bakker et al. [2015]* and can partly be explained by the relatively longer time the infragravity waves receive energy from sea-swell waves when propagating on gentle slopes. In addition, infragravity waves can dominate in the inner surf zone and swash zone of a gently sloping beach because sea-swell waves have dissipated a large part of their energy already in the wide surf zone affronting it, whereas on steep slopes sea-swell waves retain their energy up to close to the shoreline.

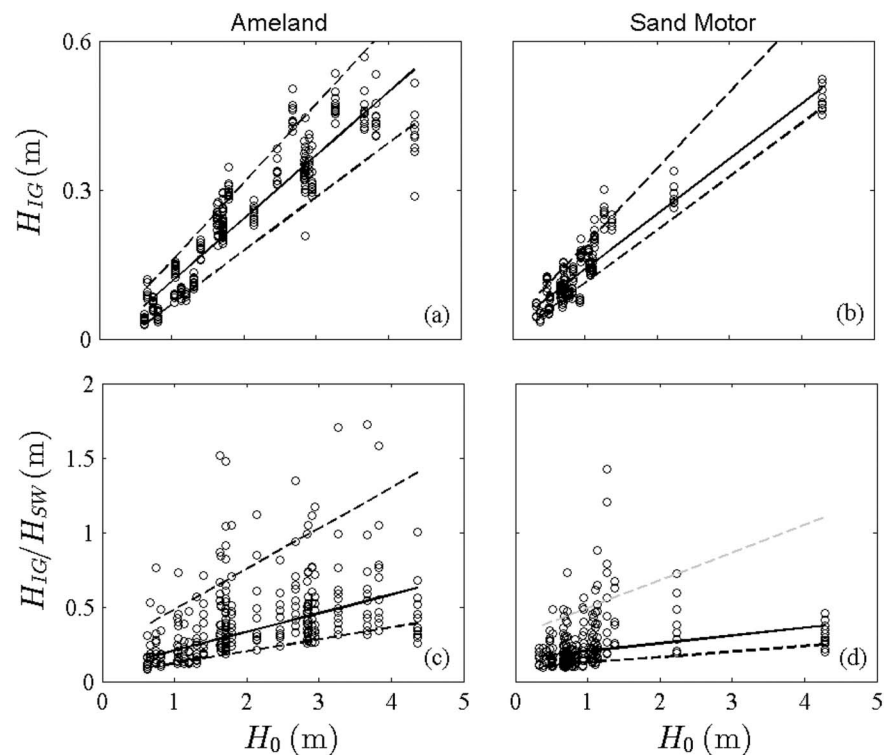


Figure 3. (a and b) Significant infragravity-wave height H_{IG} versus offshore significant sea-swell wave height H_0 and (c and d) H_{IG}/H_{SW} versus H_0 at Ameland (Figures 3a and 3c) and the Sand Motor (Figures 3b and 3d). Data from all locations including the PTs are shown for the selected tides. The lower dashed, solid, and upper dashed lines are the 10%, 50%, and 90% quantile regression lines (i.e., $\tau = 0.1, 0.5,$ and 0.9). When the slope is statistically significant (90% confidence level), the line color is black; otherwise, it is gray.

Based on simulations with the *Battjes and Janssen* [1978] wave model, the Ameland transect was completely located within the surf zone during 86% of the 29 selected high tides. Here the seaward edge of the surf zone was taken as 85% of the offshore energy flux. For less energetic conditions, the most seaward located pressure sensors of the transect were in the shoaling zone. At the Sand Motor, the instrument transect was completely positioned in the surf zone during only 24% of the 29 tides. However, the most seaward located frame was positioned within the surf zone during 69% of the selected high tides, and also here, the most onshore positioned sensors were always located in the surf zone. This gives us substantial overlap between surf zone conditions at Ameland and the Sand Motor.

3. Results

Figure 4 shows the sand flux components versus the combined infragravity and sea-swell relative wave height H_{total}/h at the gently sloping Ameland and the more steeply sloping Sand Motor. Quantile regression lines for $\tau = 0.1, 0.5,$ and 0.9 are also shown on the scatterplots to clarify whether trends are statistically significant. At the Sand Motor, the total sand fluxes are offshore directed and increases considerably when $H_{total}/h > 0.5$, probably due to the initiation of breaking of sea-swell waves, which according to the *Battjes and Janssen* [1978] wave model would start at a campaign-averaged $H_{total}/h \approx 0.48$ (Figure 4h). The mean fluxes give the largest contribution to the total sand fluxes (campaign averaged contribution of 70%) and also increase for $H_{total}/h > 0.6$ (Figure 4f). Only a minor part of the total flux is composed of the oscillatory sea-swell (19%) and infragravity (11%) components (Figures 4b and 4d). The fluxes at sea-swell and infragravity frequencies are directed both offshore and onshore and do not show a strong variability with H_{total}/h . The total sand flux at Ameland (Figure 4d) is also offshore directed and of the same order of magnitude as the Sand Motor and increases strongly for $H_{total}/h > 0.5$, when according to the *Battjes and Janssen* [1978] wave model the surf zone would be reached (campaign averaged value of $H_{total}/h \approx 0.53$) (Figure 4h). However, the mean component contributes less to the total sand flux (59%, Figure 4e), due to the weaker undertow present here, which confirms earlier findings that for given wave conditions the undertow is weaker on more gently

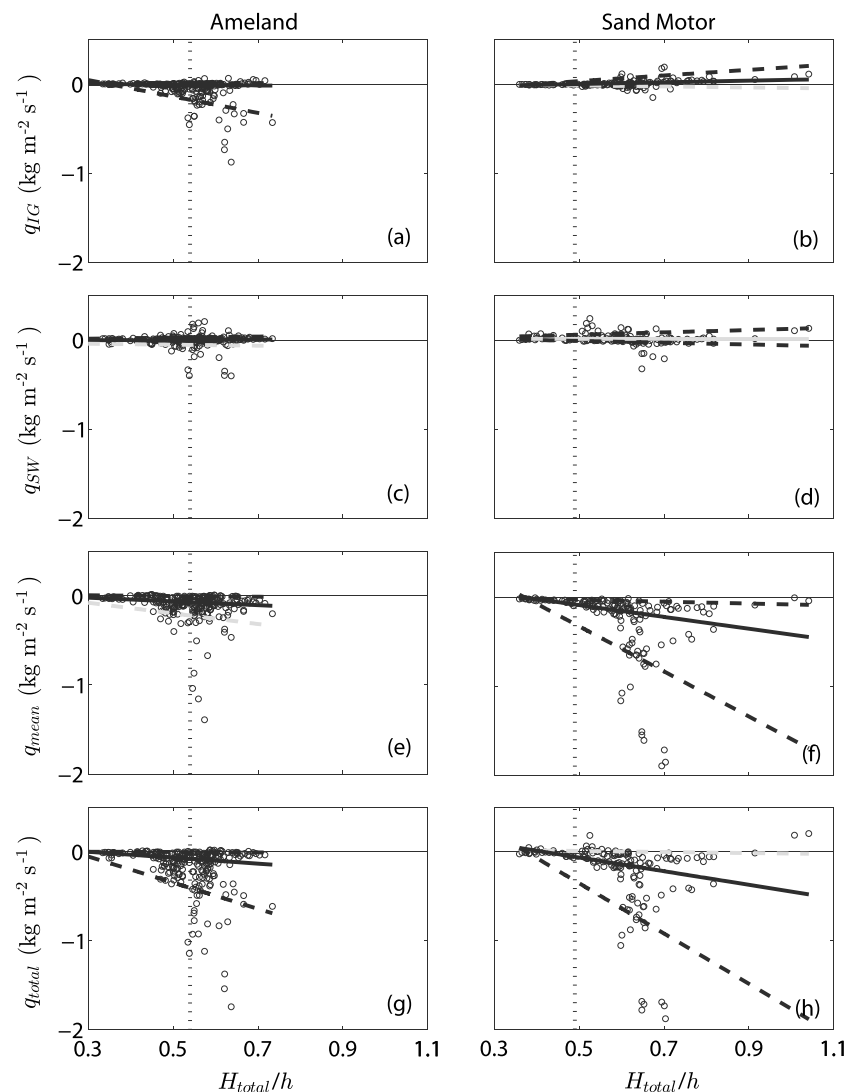


Figure 4. (a and b) Infragravity-wave sand flux rate q_{IG} , (c and d) sea-swell wave sand flux rate q_{SW} , (e and f) mean sand flux rate q_{mean} , and (g and h) total sand flux rate q_{total} versus relative significant wave height H_{total}/h , for Ameland (Figures 4a, 4c, 4e, and 4g) and the Sand Motor (Figures 4b, 4d, 4f, and 4h). The vertical dashed line indicates the campaign-averaged edge of the surf zone according to the Battjes and Janssen [1978] wave model. The lower dashed, solid, and upper dashed lines are the 10%, 50%, and 90% quantile regression lines (i.e., $\tau = 0.1, 0.5$, and 0.9). When the slope is statistically significant (90% confidence level), the line color is black; otherwise, it is gray.

sloping beaches [Longuet-Higgins, 1983; Aagaard et al., 2002]. On the contrary, the infragravity-wave component (20%) is considerably larger than at the Sand Motor and is predominantly offshore directed (Figure 4a). The sea-swell component is contributing least (21%) to the total sand flux and is directed both onshore and offshore (Figure 4b).

At the Sand Motor, r_0 ranged between -0.5 and 0.3 (Figure 5a). Offshore-directed q_{IG} is generally (88.9%) associated with negative r_0 and onshore-directed q_{IG} with positive r_0 (56.5%), confirming the purely hydrodynamic-based theory of Abdelrahman and Thornton [1987] and Roelvink and Stive [1989]. An unpaired two-sample t test, assuming unequal variance, confirms that the mean of q_{IG} with negative r_0 is different from the mean q_{IG} with positive r_0 ($p < 0.0001$). For Ameland all r_0 are generally between -0.3 and 0.3 (Figure 5b); more negative r_0 presumably occurred seaward of our array, and the infragravity waves at the array were no longer predominantly bound waves. Even for positive r_0 , q_{IG} is offshore directed and is on average 4 times larger than at the Sand Motor. Whereas r_0 can predict the sign of q_{IG} at the rather steep sloping Sand Motor, this is not the case for the gently sloping Ameland site.

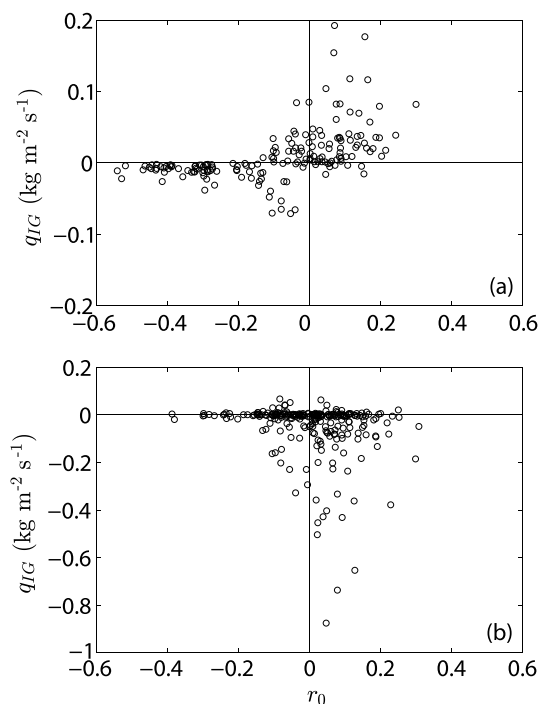


Figure 5. Correlation coefficient r_0 versus infragravity sand flux q_{IG} at (a) the Sand Motor and (b) Ameland.

An example of a sand concentration time series in the shoaling zone with negative r_0 is shown in Figure 6a, together with the cross-shore velocity time series of the total and infragravity signals (Figure 6b). The suspension events peak at sea-swell frequencies when the sea-swell wave envelope is highest. In other words, wave stirring is modulated at the infragravity timescale, with most sand in suspension during negative orbital infragravity motion u_{IG} , consistent with earlier observations seaward of the surf zone [Larsen, 1982; Huntley and Hanes, 1987; Osborne and Greenwood, 1992; Ruessink et al., 1998a; Smith and Mocke, 2002]. The cospectrum of c and u shows that almost all infragravity frequencies show a negative (offshore) flux (Figure 6c). An example for positive r_0 in the surf zone is shown in Figure 7. Also, here sand is suspended by the sea-swell waves and events cluster together (Figure 7a). Although infragravity velocities are considerably stronger than shown in Figure 6, and negative u_{IG} are stronger than the positive u_{IG} (skewness of -0.37), still most sand suspends

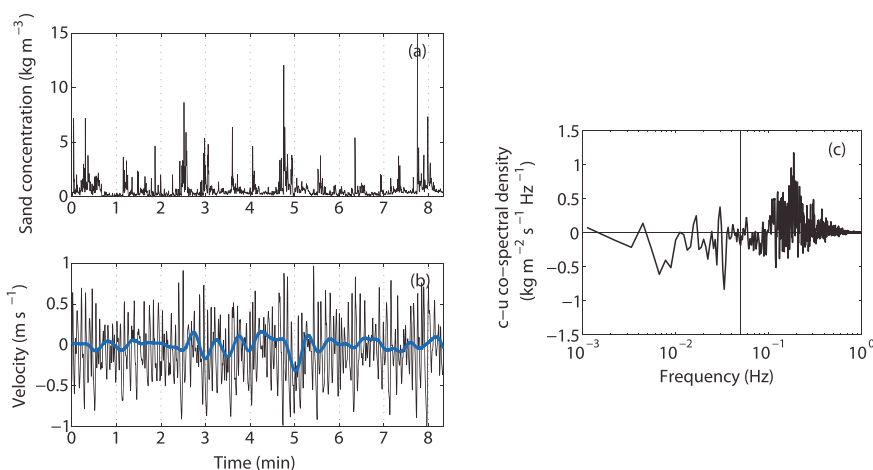


Figure 6. (a and b) Example time series and (c) cospectral density of c and u for negative r_0 at the Sand Motor. Sand concentration (Figure 6a) and cross-shore velocity (Figure 6b) with in black the total velocity and in blue the infragravity velocity. The black vertical line in Figure 6c is the separation between infragravity and sea-swell frequencies. P_5 , $h = 1.3$ m, $r_0 = -0.42$, relative water depth $H_{total}/h = 0.46$, $\bar{u} = -0.06$ m/s, and $H_{IG}/H_{SW} = 0.17$.

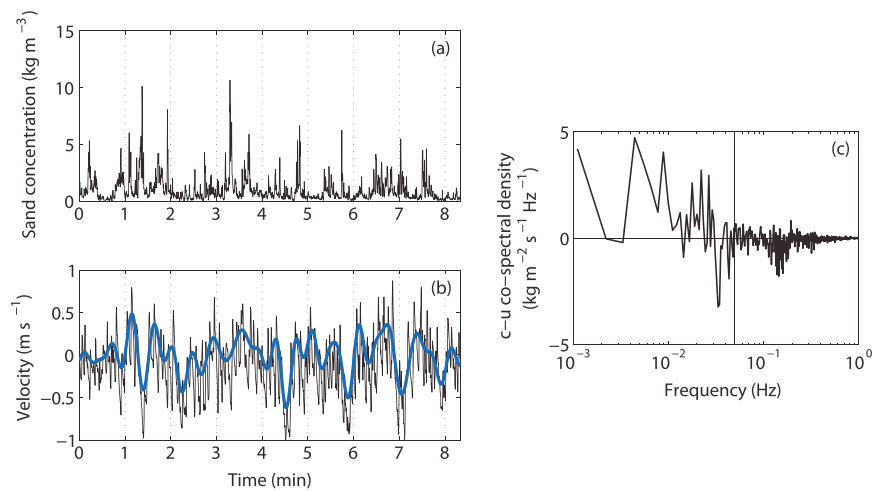


Figure 7. (a and b) Example time series and (c) cospectral density of c and u for negative r_0 at the Sand Motor. Sand concentration (Figure 7a) and cross-shore velocity (Figure 7b) with in black the total velocity and in blue the infragravity velocity. The black vertical line in Figure 7c is the separation between infragravity and sea-swell frequencies. P10, $h = 0.5$ m, $r_0 = 0.17$, $H_{total}/h = 0.66$, and $\bar{u} = -0.16$ m/s, $H_{IG}/H_{SW} = 0.39$.

during positive u_{IG} because of the energetic sea-swell waves present there (Figure 7b). Almost all frequencies in the infragravity band show a positive (onshore) flux. Figure 8 shows an example time series of sand suspension events in the surf zone during an energetic high tide at Ameland with $H_{IG}/H_{SW} \approx 1$. Irrespective of the location of the largest sea-swell waves ($r_0 = -0.04$), sand is predominantly suspended under negative u_{IG} . The u_{IG} is only mildly skewed (-0.25) and asymmetric (-0.17), and thus infragravity-induced shear stresses under the trough and crest should be about equal in strength. The undertow (here $\bar{u} \approx -0.15$ m/s) is hypothesized to enhance negative u_{IG} , and hence shear stresses, while counteracting the positive u_{IG} and associated shear stresses, leading to predominant sand stirring for negative u_{IG} . A similar role for undertow in modifying sand suspension was demonstrated for shear waves and asymmetric short waves by Miles *et al.* [2002] and Ruessink *et al.* [2011], respectively.

Figure 9a indicates that r_0 is predominantly negative when H_{IG}/H_{SW} is smaller than ≈ 0.3 (where the quantile regression line for $\tau = 0.5$ intersects with the x axis) and slightly positive for $0.3 < H_{IG}/H_{SW} < 0.4$. As mentioned before in section 2, H_{IG}/H_{SW} at the Sand Motor is considerably smaller (0.1–0.5) than at Ameland

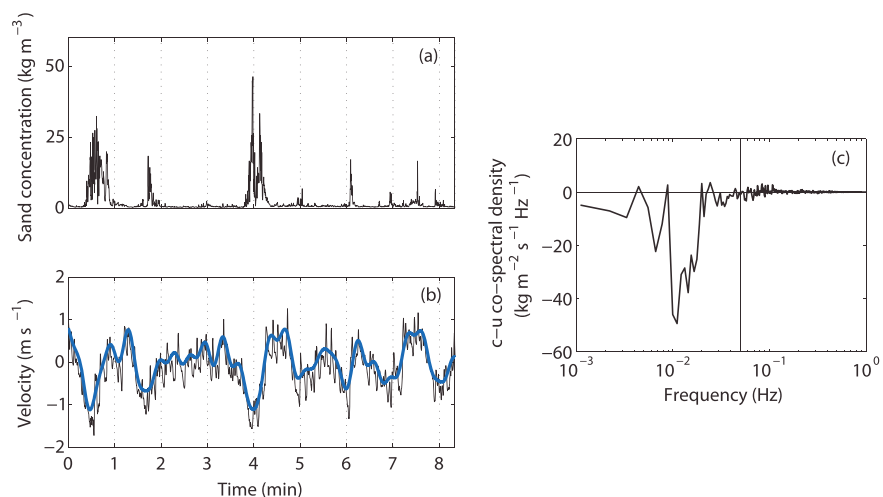


Figure 8. (a and b) Example time series and (c) cospectral density of c and u for an energetic high tide at Ameland. Sand concentration (Figure 8a) and cross-shore velocity (Figure 8b) with in black the total velocity and in blue the infragravity velocity. The black vertical line in Figure 8c is the separation between infragravity and sea-swell frequencies. P11, $h = 1.00$ m, $r_0 = -0.04$, $H_{total}/h = 0.67$, $\bar{u} = -0.15$ m/s, and $H_{IG}/H_{SW} = 1.00$.

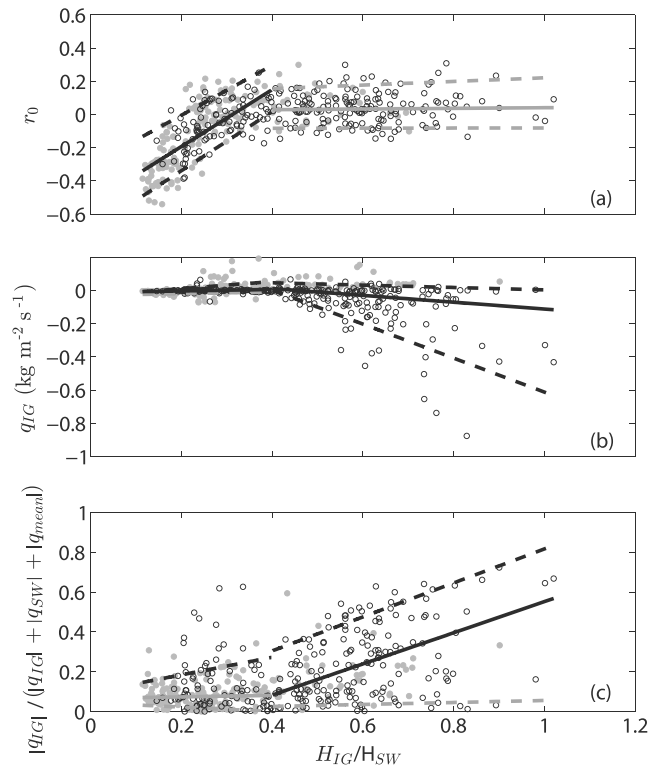


Figure 9. (a) Correlation coefficients r_0 (b) sand flux rate at infragravity frequencies q_{IG} , and (c) relative contribution of the infragravity-wave component to the total sand flux $|q_{IG}|/(|q_{IG}| + |q_{SW}| + |q_{mean}|)$, versus relative infragravity-wave height H_{IG}/H_{SW} . Black circles for Ameland and grey dots for the Sand Motor. The lower dashed, solid, and upper dashed lines are the 10%, 50%, and 90% quantile regression lines (i.e., $\tau = 0.1, 0.5,$ and 0.9). When the slope is statistically significant (90% confidence level), the line color is black; otherwise, it is gray.

(0.2–1), but the trends with r_0 overlap. Quantile regression for $H_{IG}/H_{SW} > 0.4$ indicates that r_0 does not depend on H_{IG}/H_{SW} anymore and is also not statistically different from zero. As shown in Figure 9b, q_{IG} increases strongly for $H_{IG}/H_{SW} > 0.4$ and is then predominantly directed offshore. For small H_{IG}/H_{SW} , q_{IG} contributes <20% to q_{total} (Figure 9c); with an increase in H_{IG}/H_{SW} , q_{IG} not only increases in magnitude (Figure 9a) but also accounts for a considerable larger part of the q_{total} (up to 60%, see Figure 9c).

Although larger H_{IG}/H_{SW} corresponds to an overall larger offshore-directed q_{IG} , there is substantial variability for the same H_{IG}/H_{SW} . Part of this variability can be explained by the infragravity wave height itself, as during more energetic conditions infragravity-wave fluxes increase. In other words, large q_{IG} demand both large H_{IG} and H_{IG}/H_{SW} and are thus inherently limited to inner surf conditions during storms on a gently sloping beach. However, variations in instrument height and a number of other factors also contribute to the variability in q_{IG} . As a reliable quantification of these errors cannot be given, we can focus on general trends, as quantified with quantile regression, only.

4. Discussion

4.1. Instrument Height

In our analysis we have focused on sand flux rates at 0.03–0.1 m above the bed. We chose to restrict the measurements to this range because we expect the largest part of the suspended sand fluxes to take place relatively close to the bed. When the instrument height selection was restricted further (say 0.03–0.05 m), the available data became too scarce for meaningful analyses. We realize that higher in the water column, sand concentrations are lower and potentially lag those closer to the bed, possibly affecting the magnitude, sign, and relative importance of q_{IG} . Figure 10a shows relatively large correlations (≈ 0.8) between the instantaneous sediment concentration signals filtered on infragravity frequencies of the OBS located between 0.03 and 0.1 m above the bed and a second OBS, located roughly between 0.1 and 0.2 m, indicating that suspension peaks consistently spread higher up into the water column. However, correlations drop for the Ameland

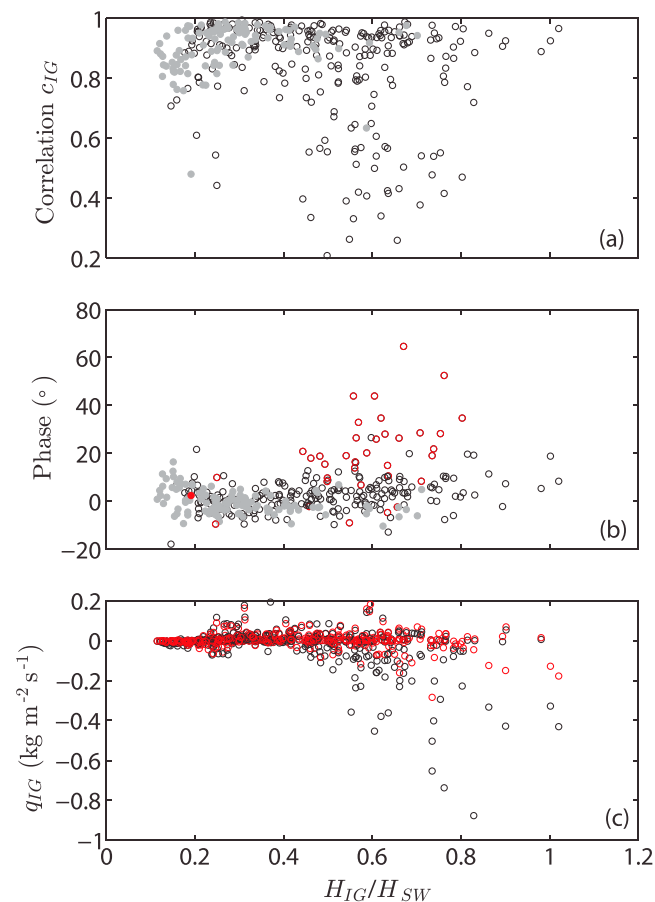


Figure 10. (a) Correlation between the infragravity-scale concentrations in the OBS used in results c_{IG} , and the OBS positioned above that, versus H_{IG}/H_{SW} , for the Sand Motor (grey dots) and Ameland (black circles). (b) Phase θ between the two OBSs versus H_{IG}/H_{SW} , for the Sand Motor (grey dots) and Ameland (black circles) with in red the moments when the correlation is lower than 0.6. (c) Sand flux rate at infragravity frequencies q_{IG} versus H_{IG}/H_{SW} , with in black data used in the results, and in red data for the OBS above that.

data set when the sensor height of the upper OBS exceeds 0.15 m, possibly because these measurements were then taken above the sand suspension layer. Phase lags were determined by calculating the phase of a cross-power-spectral density analysis of the two instantaneous concentration signals and a subsequent averaging over the infragravity wave band. Figure 10b shows that the phase lag between the two concentration signals (where correlations are above 0.6) is $\approx 0^\circ$, thus showing no phase lag higher up in the water column. Figure 10c illustrates that, in general, as expected, q_{IG} are smaller higher in the water column, but the dependence on H_{IG}/H_{SW} is similar.

4.2. Conceptual Model

Overall, sand is predominantly suspended by sea-swell waves at the moderately sloping Sand Motor beach, when H_{IG} is both small in absolute and relative ($H_{IG}/H_{SW} < 0.4$) sense. The infragravity-wave flux direction is related to the presence of the larger sea-swell waves with negative u_{IG} ($r_0 < 0$), inducing offshore q_{IG} , or with positive u_{IG} ($r_0 > 0$), inducing onshore q_{IG} (Figure 11a). In general, the q_{IG} is small and accounts for less than 20% of the total flux, even during storm conditions. Negative r_0 is typical of the shoaling and outer surf zone, while r_0 is positive farther landward, in the inner surf zone. In the gently sloping inner surf zone at Ameland, H_{IG}/H_{SW} can increase to over 0.4, which, probably in combination with the undertow, leads to infragravity-scale sand suspension during negative u_{IG} (Figure 11b). Now during high energetic conditions, q_{IG} can contribute considerably to the total sand flux, up to 60%. We hypothesize that this modulation is small or even absent on steep slopes, because the sea-swell waves dominate the water motion up to the shoreline, and H_{IG} remains relatively small.

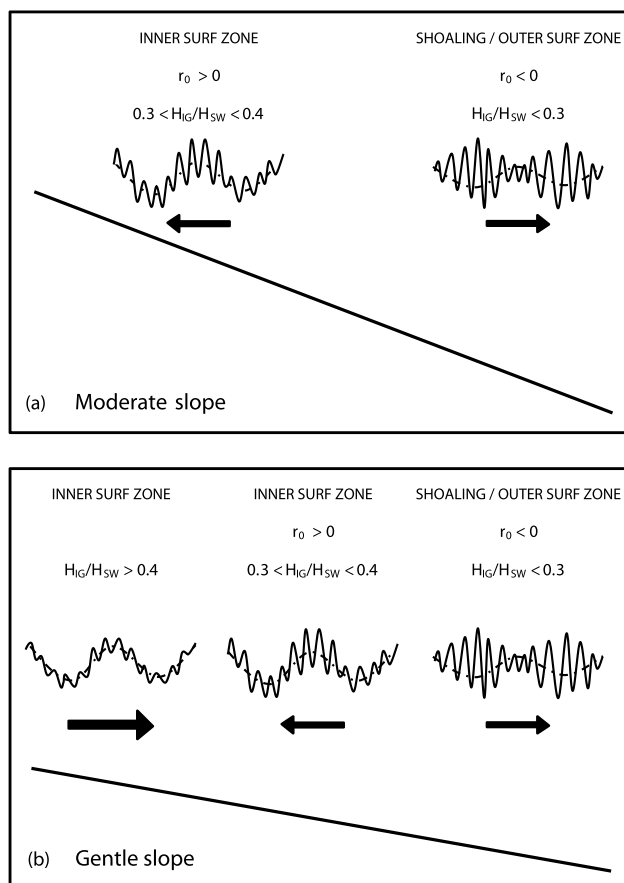


Figure 11. Conceptual figure for sand suspension mechanisms and resulting infragravity-wave flux directions for (a) a moderately sloping beach and (b) a gently sloping beach. Note that the size of the smallest waves for negative r_0 is similar to the largest waves for positive r_0 . The magnitude of the arrows might change with height above the bed, but the direction is not expected to change, based on the results of section 4.1.

Acknowledgments

The field data can be made available upon request from the first author (a.t.m.debakker@uu.nl). This work was funded by the Netherlands Organisation for Scientific Research (NWO) under contract 821.01.012. J.B. was funded by the Dutch Technology Foundation STW that is part of the Netherlands Organisation for Scientific Research (NWO) and which is partly funded by the Ministry of Economic Affairs (project 12397). We thank Marcel van Maarsseveen, Henk Markies, Chris Roosendaal, Bas van Dam, Aline Pieterse, Emily McCullough, Jantien Rutten, Marieke Dirksen, and Laura Brakenhoff for their assistance in the field. Without you, this study would not have been possible. The discussions with Renske de Winter, Jasper Donker, Jantien Rutten, and Timothy Price during the initial stage of this work helped to direct the analysis. Furthermore, we want to thank Troels Aagaard, Giovanni Coco, the Associate Editor, and an anonymous reviewer for their constructive comments.

5. Conclusions

Measurements of near-bed velocity and sand concentrations were collected at up to four locations in the intertidal zone on a moderately and a gently sloping beach. On the whole, our data show that the local ratio of infragravity to sea-swell wave height is a good proxy for the infragravity-related sand suspension mechanism, the infragravity flux direction, and the relative importance of infragravity waves to the total cross-shore sand flux. On the moderately sloping beach, infragravity waves are typically small compared to sea-swell waves ($H_{IG}/H_{SW} < 0.4$), despite offshore wave heights close to 5 m. Accordingly, the sand is suspended by the sea-swell waves, and the infragravity flux direction is linked to the correlation r_0 of the infragravity orbital motion with the sea-swell wave envelope. In the shoaling and outer surf zone, the largest sea-swell waves are present during negative u_{IG} , leading to an offshore-directed infragravity flux. Farther shoreward, r_0 becomes positive as the largest sea-swell waves are present during positive u_{IG} , resulting in onshore infragravity flux. However, in both cases the infragravity flux hardly contribute to the total flux (<20%). This contrasts with the inner surf zone of the gently sloping beach, where the infragravity waves are more energetic ($H_{IG}/H_{SW} > 0.4$), and their flux contribution is substantial (up to 60% during storms). Irrespective of sea-swell wave location ($r_0 \approx 0$), the infragravity flux is predominantly offshore directed as the sand is mostly suspended during negative u_{IG} . As the infragravity wave shape is then neither skewed nor asymmetric, the suspension of sand was probably enhanced during negative u_{IG} by sea-swell waves and/or the undertow.

References

Aagaard, T., and B. Greenwood (2008), Infragravity wave contribution to surf zone sediment transport—The role of advection, *Mar. Geol.*, 251, 1–14, doi:10.1016/j.margeo.2008.01.017.
 Aagaard, T., K. P. Black, and B. Greenwood (2002), Cross-shore suspended sediment transport in the surf zone: A field-based parameterization, *Mar. Geol.*, 185, 283–302, doi:10.1016/j.margeo.2010.02.019.

- Aagaard, T., B. Greenwood, and M. Hughes (2013), Sediment transport on dissipative, intermediate and reflective beaches, *Earth Sci. Rev.*, *124*, 32–50, doi:10.1016/j.earscirev.2013.05.002.
- Abdelrahman, S. M., and E. B. Thornton (1987), Changes in the short wave amplitude and wavenumber due to the presence of infragravity waves, in *Proceedings of the Specialty Conference on Coastal Hydrodynamics*, edited by R. A. Dalrymple, pp. 458–478, Am. Soc. of Civ. Eng., New York.
- Alsina, J. M., and I Cáceres (2011), Sediment suspension events in the inner surf and swash zone. Measurements in large-scale and high-energy wave conditions, *Coastal Eng.*, *58*, 657–670, doi:10.1016/j.coastaleng.2011.03.002.
- Baldock, T. E., P. Manoonvoravong, and K. S. Pham (2010), Sediment transport and beach morphodynamics induced by free long waves, bound long waves and wave groups, *Coastal Eng.*, *57*, 898–916, doi:10.1016/j.coastaleng.2010.05.006.
- Battjes, J. A., and J. P. F. M. Janssen (1978), Energy loss and set-up due to breaking of random waves, in *Proceedings of the 16th International Conference on Coastal Engineering*, pp. 570–587, ASCE, Hamburg, Germany.
- Beach, R. A., and R. W. Sternberg (1988), Suspended sediment transport in the surf zone: Response to cross-shore infragravity motion, *Mar. Geol.*, *80*, 61–79.
- Bunt, J. A. C., P. Larcombe, and C. F. Jago (1999), Quantifying the response of optical backscatter devices and transmissometers to variations in suspended particulate matter, *Cont. Shelf Res.*, *19*, 1199–1220.
- Cade, B. S., and B. R. Noon (2003), A gentle introduction to quantile regression for ecologists, *Front. Ecol. Environ.*, *1*(8), 412–420, doi:10.1890/1540-9295(2003)001[0412:AGITQR]2.0.CO;2.
- Conley, D. C., and R. A. Beach (2003), Cross-shore sediment transport partitioning in the nearshore during a storm event, *J. Geophys. Res.*, *108*(C3), 3065, doi:10.1029/2001JC001230.
- Conner, C. S., and A. M. De Visser (1992), A laboratory investigation of particle size effects on an optical backscatterance sensor, *Mar. Geol.*, *108*, 151–159.
- De Bakker, A. T. M., M. F. S. Tissier, and B. G. Ruessink (2014), Shoreline dissipation of infragravity waves, *Cont. Shelf Res.*, *72*, 73–82, doi:10.1016/j.csr.2013.11.013.
- De Bakker, A. T. M., M. F. S. Tissier, and B. G. Ruessink (2015), Beach steepness effects on nonlinear infragravity-wave interactions: A numerical study, *J. Geophys. Res. Oceans*, *121*, 554–570, doi:10.1002/2015JC011268.
- De Schipper, M. A., S. De Vries, B. G. Ruessink, R. C. De Zeeuw, J. Rutten, C. Van Gelder-Maas, and M. J. F. Stive (2016), Initial spreading of a mega feeder nourishment: Observations of the Sand Engine pilot project, *Coastal Eng.*, *111*, 23–38, doi:10.1016/j.coastaleng.2015.10.011.
- Elgar, S., E. L. Gallagher, and R. T. Guza (2001), Nearshore sandbar migration, *J. Geophys. Res.*, *106*, 11,623–11,627.
- Gallagher, E. L., S. Elgar, and R. T. Guza (1998), Observations of sand bar evolution on a natural beach, *J. Geophys. Res.*, *103*, 3203–3215.
- Guza, R. T., and E. B. Thornton (1982), Swash oscillations on a natural beach, *J. Geophys. Res.*, *87*, 483–491.
- Houser, C., and B. Greenwood (2005), Hydrodynamics and sediment transport within the inner surf zone of a lacustrine multiple-barred nearshore, *Mar. Geol.*, *218*, 37–63, doi:10.1016/j.margeo.2005.02.029.
- Huntley, D. A., and D. M. Hanes (1987), Direct measurements of suspended sediment transport, in *Proceedings of Coastal Sediments '87*, edited by N. C. Kraus, pp. 723–737, ASCE, New York.
- King, D. B. (1991), Studies in oscillatory flow bedload sediment transport, PhD thesis, Univ. of Calif., San Diego, Calif.
- Koenker, R. (2005), *Quantile Regression*, 349 pp., Cambridge Univ. Press, New York.
- Kularatne, S., and C. Pattiaratchi (2014), The role of infragravity waves in near-bed cross-shore sediment flux in the breaker zone, *J. Mar. Sci. Eng.*, *2*, 568–592, doi:10.3390/jmse20300568.
- Lancaster, P., and K. Šaulkauskas (1996), *Transform Methods in Applied Mathematics*, 332 pp., John Wiley, New York.
- Larsen, L. (1982), A new mechanism for seaward dispersion of midshelf sediments, *Sedimentology*, *29*, 279–283.
- Lippmann, T. C., T. H. C. Herbers, and E. B. Thornton (1999), Gravity and shear wave contributions to nearshore infragravity motions, *J. Phys. Oceanogr.*, *29*, 231–239.
- Longuet-Higgins, M. S. (1983), Wave set-up, percolation and undertow in the surf zone, *Proc. R. Soc. A*, *390*, 283–291.
- Ludwig, K. A., and D. M. Hanes (1990), A laboratory evaluation of optical backscatterance suspended solids sensors exposed to sand-mud mixtures, *Mar. Geol.*, *94*, 173–179.
- Miles, J. (2013), Wave shape effects on sediment transport, *J. Coastal Res.*, *2*(65), 1803–1808, doi:10.2112/SI65-305.1.
- Miles, J. R., P. E. Russell, B. G. Ruessink, and D. A. Huntley (2002), Field observations of the effect of shear waves on sediment transport and flux, *Cont. Shelf Res.*, *22*, 657–681.
- Osborne, P. D., and B. Greenwood (1992), Frequency dependent cross-shore suspended sediment transport. 2. A barred shoreface, *Mar. Geol.*, *106*, 25–51.
- Puleo, J., R. Johnson, T. Butt, T. N. Kooney, and K. T. Holland (2006), The effect of air bubbles on optical backscatter sensors, *Mar. Geol.*, *230*, 87–97, doi:10.1016/j.margeo.2006.04.008.
- Roelvink, J. A., and M. J. F. Stive (1989), Bar-generating cross-shore flow mechanisms on a beach, *J. Geophys. Res.*, *94*, 4785–4800.
- Ruessink, B. G., K. T. Houwman, and P. Hoekstra (1998a), The systematic contribution of transporting mechanisms to the cross-shore sediment flux in water depths of 3 to 9 m, *Mar. Geol.*, *152*, 295–324.
- Ruessink, B. G., M. G. Kleinhans, and P. G. L. Van den Beukel (1998b), Observations of swash under highly dissipative conditions, *J. Geophys. Res.*, *103*, 3111–3118.
- Ruessink, B. G., I. M. J. Van Enckevort, K. S. Kingston, and M. A. Davidson (2000), Analysis of observed two- and three-dimensional nearshore bar behaviour, *Mar. Geol.*, *169*, 161–183.
- Ruessink, B. G., H. Michallet, T. Abreu, F. Sancho, D. A. van der A, J. J. van der Werf, and P. A. Silva (2011), Observations of velocities, sand concentrations, and fluxes under velocity-asymmetric oscillatory flows, *J. Geophys. Res.*, *116*, C03004, doi:10.1029/2010JC006443.
- Ruessink, B. G., M. Boers, P. van Geer, A. de Bakker, A. Pieterse, F. Grasso, and R. de Winter (2012), Towards a process-based model to predict dune erosion along the Dutch Wadden coast, *Neth. J. Geosci.*, *91*(3), 357–372.
- Russell, P. (1993), Mechanisms for beach erosion during storm, *Cont. Shelf Res.*, *13*, 1243–1265.
- Sénéchal, N., G. Coco, K. R. Bryan, and R. A. Holman (2011), Wave runup during extreme storm conditions, *J. Geophys. Res.*, *116*, C07032, doi:10.1029/2010JC006819.
- Shibayama, T., E. Saito, and A. Okayasu (1991), Effect of long waves to local sediment transport rate, in *Coastal Sediments '91. Proceedings of a speciality conference on quantitative approaches to coastal sediment processes, Seattle, Washington, 25-27 Jun.*, edited by N. C. Kraus, K. J. Gingerich, and D. L. Kriebel, pp. 129–138, ASCE, New York.
- Smith, G., and G. P. Mocke (2002), Interaction between breaking/broken waves and infragravity-scale phenomena to control sediment suspension transport in the surf zone, *Mar. Geol.*, *187*, 329–345.

- Tissier, M. F. S., P. Bonneton, H. Michallet, and B. G. Ruessink (2015), Infragravity-wave modulation of short-wave celerity in the surf zone, *J. Geophys. Res. Oceans*, *120*, 6799–6814, doi:10.1002/2015JC010708.
- Van der A, D. A., T. O'Donoghue, and J. S. Ribberink (2010), Measurements of sheet flow transport in acceleration-skewed oscillatory flow and comparison with practical formulations, *Coastal Eng.*, *57*, 331–342, doi:10.1016/j.coastaleng.2009.11.006.
- Van Thiel de Vries, J. S. M., M. R. A. van Gent, D. J. R. Walstra, and A. J. H. M. Reniers (2008), Analysis of dune erosion processes in large-scale flume experiments, *Coastal Eng.*, *55*(12), 1028–1040, doi:10.1016/j.coastaleng.2008.04.004.
- Walstra, D. J., D. Wesselman, E. van der Deijl, and G. Ruessink (2016), On the intersite variability in inter-annual nearshore sandbar cycles, *J. Mar. Sci. Eng.*, *4*(1), 15, doi:10.3390/jmse4010015.